Available online at www.sciencedirect.com
SCIENCE DIRECT®
International Journal of Heat and Mass Transfer 48 (2005) 2943–2954
International Journal of HEAT and MASS TRANSFER
www.elsevier.com/locate/ijhmt

Conduction and entrance effects on laminar liquid flow and heat transfer in rectangular microchannels

Gabriel Gamrat [a], Michel Favre-Marinet [b,*], Dariusz Asendrych [a]

[a] Institute of Thermal Machinery, Czestochowa University of Technology, Al. Armii Krajowej 21, 42-200 Czestochowa, Poland
[b] Laboratoire des Ecoulements Géophysiques et Industriels, CNRS-UJF-INPG, 1025 rue de la Piscine, BP 53 X, 38041 Grenoble Cedex, France

Received 22 March 2004; received in revised form 10 September 2004

Abstract

The paper presents both three and two-dimensional numerical analysis of convective heat transfer in microchannels. The three-dimensional geometry of the microchannel heat sink followed the details of the experimental facility used during a previous research step. The heat sink consisted of a very high aspect ratio rectangular microchannel. Two channel spacings, namely 1 mm and 0.3 mm (0.1 mm), were used for three-dimensional (two-dimensional) numerical model, respectively. Water was employed as the cooling liquid. The Reynolds number ranged from 200 to 3000. In the paper, thermal entrance effects and conduction/convection coupling effects are considered both for the test case of uniform channel inlet conditions and the complete geometry of the experiment. Finally, the comparison between measured and computed heat flux and temperature fields is presented. Contrary to the experimental work, the numerical analysis did not reveal any significant scale effect on heat transfer in microchannel heat sink down to the smallest size considered (0.1 mm).

Keywords: Microheat transfer; Microchannel; Conjugated heat transfer; Numerical analysis

1. Introduction

Microchannel heat sinks are of special interest as high efficiency cooling devices due to undeniable advantages such as small coolant demand and dimensions, which directly result in enhanced convective heat transfer. As a result, much work in recent years has gone into the development of microchannel technology. Enhancement of the heat transfer coefficient is obviously required along with a reduction in length scales. This has been observed many times since the first experiments of Tuckerman and Pease [1]. These practical advantages of microchannel heat sinks have stimulated a strong current of research from experimental, theoretical and also numerical points of view in the last ten years. A comprehensive survey may be found in [2].

Experimental studies on microchannel heat transfer reported in the literature present a strong dispersion of results [2] and sometimes disagree with the conventional theories of transport phenomena which are well verified in macroscale flows. If we restrict the discussion to the laminar regime of liquid flows, several experimental

* Corresponding author. Tel.: +33 4 76 82 50 49; fax: +33 4 76 82 52 71.
E-mail addresses: g.gamrat@imc.pcz.czest.pl (G. Gamrat), michel.favre-marinet@hmg.inpg.fr (M. Favre-Marinet), darek@imc.pcz.czest.pl (D. Asendrych).

0017-9310/$ - see front matter © 2004 Elsevier Ltd. All rights reserved.
doi:10.1016/j.ijheatmasstransfer.2004.10.006

Nomenclature

c	specific heat, $J\,kg^{-1}\,K^{-1}$
c_p	specific heat at constant pressure, $J\,kg^{-1}\,K^{-1}$
D_h	hydraulic diameter, m
e	microchannel spacing, mm
e^*	dimensionless spacing (Eq. (6))
e_s	lengthscale for longitudinal conduction, mm
f	fanning friction factor
h	convection heat transfer coefficient, $W\,m^{-2}\,K^{-1}$
L	channel length, mm
L^+	non-dimensional channel length
Nu	Nusselt number
p	pressure, $N\,m^{-2}$
Δp	pressure drop over the distance x, $N\,m^{-2}$
Po	Poiseuille number
Pr	Prandtl number
R	radius of quarter cylinder at channel entrance, mm
Re	Reynolds number
T	temperature, K
$\vec{V}$	velocity vector, $m\,s^{-1}$
V_b	bulk velocity, $m\,s^{-1}$
x	abscissa along the channel, m
y	coordinate in the direction perpendicular to the channel walls, m
x^+	dimensionless developing length (Eq. (13))
x^*	entrance region parameter (Eq. (9))

Greek symbols

δ_0	boundary layer thickness at channel inlet, m
θ	dimensionless temperature (Eq. (16))
λ	thermal conductivity, $W\,m^{-1}\,K^{-1}$
ρ	density, $m^3\,s^{-1}$
μ	dynamic viscosity, $kg\,m^{-1}\,s^{-1}$
φ	heat flux, $W\,m^{-2}$
Φ	total heat flux, W

Subscripts and abbreviations

exp	experimental
f	fluid
in	inlet
lam	laminar
num	numerical
s	solid
w	wall

studies [3–6] indicate two different trends when compared to heat transfer in channels of conventional size:

(1) variation of the Nusselt number with the Reynolds number,
(2) reduction in the Nusselt number with the microchannel size.

For example, these two features may be observed in the results of Peng et al. [3] on heat transfer in rectangular microchannels, ranging from 0.133 mm to 0.343 mm in hydraulic diameter. The same observation may be done about the results of Celata et al. [5] in the laminar regime of 0.130 mm for capillary tube flows. On the contrary, Qu et al. [4] found *Re*-independent values of the Nusselt number in trapezoidal silicon microchannels. However, they found very low values of Nu ($\approx$1–2) in these microchannels, ranging from 62 μm to 169 μm in hydraulic diameter.

It is likely that the first feature corresponds, at least partly, to entrance effects, which may be important in the laminar regime. The second one has not received a definite explanation. It must be underlined that experiments in microchannels are extremely difficult due to the small size of the test sections. This is especially true for heat transfer measurements. There is no direct measurement of heat flux at the fluid-solid interface in published studies. Moreover, wall temperature measurements are performed at some distance away from this interface. As a result, it is difficult to directly deduce the Nusselt number from the measurements so that the experimental data must be carefully interpreted. Several assumptions are usually made to infer unknown quantities from the measured ones. Among them, the wall heat flux is assumed in most studies to be uniformly distributed over the fluid/solid surface when the heat source is supplied electrically, which may be far from the actual boundary conditions. Numerical modeling of the fluid flow and associated heat transfer may be a very helpful tool to interpret experimental data and to test these assumptions. It may be also very useful to evaluate the relative importance of the physical phenomena possibly involved in microchannel heat transfer. Thus, several numerical studies considered conjugate heat transfer in microchannels. Weisberg et al. [7] performed a two-dimensional numerical analysis pertaining to Tuckerman's experiments [8], assuming both hydraulically and thermally fully developed flow within the microchannels. Toh et al. [9] extended numerical simulations to the three-dimensional case. The authors compared results obtained both for constant and temperature dependent water properties. They found that the friction coefficient decreases drastically at low Reynolds number in the heating case. This is due to large values of the water temperature, and subsequently to low values of the viscosity for small Reynolds numbers. Fedorov

and Viskanta [10] and later, Qu and Mudawar [11] compared three-dimensional numerical simulations to published experimental results.

There are few articles on experimental and numerical works performed in the same research group. Qu et al. [4] carried out a numerical analysis to solve conjugate heat transfer in a model of their trapezoidal microchannels. The authors assumed both hydraulically and thermally fully-developed regime. The computed values of *Nu* were much larger (by a factor of 2–3) than the experimental ones. The authors attributed this discrepancy to wall roughness and they introduced a modified viscosity model to account for these effects. More recently, Qu and Mudawar [12] conducted both experimental and numerical investigations of a microchannel heat sink, consisting of 21 parallel rectangular microchannels. They found good agreement of the measured temperature distributions along the channel wall with the numerical predictions based on the conventional mass, momentum and energy equations. The same conclusion was drawn by Tiselj et al. [13] in a numerical and experimental study on triangular microchannel heat transfer. The authors determined the characteristics of water flowing through triangular silicon microchannels with hydraulic diameter of 160 μm in a range of low Reynolds number (3.2–64). Lelea et al. [14] considered the heat transfer and fluid flow of distilled water in round tubes ranging from 0.1 to 0.5 mm in diameter. Their experimental and numerical analysis also showed that conventional theories are applicable in the conditions of their experiments.

It can be concluded from above discussion that the scaling laws pertaining to laminar heat transfer in microchannels are not clearly established. Some possible microscale effects were suggested by Mala et al. [15] and Guo and Li [16]. Among the possible sources of deviation from the conventional laws, effects of axial heat conduction in the walls and entrance effects in the microchannel test section are seriously suspected to contribute to the observed scale effect [16]. Peterson [17] quantified the relative importance of conduction heat transfer compared to the energy carried by the fluid in microscale heat exchangers. Recently, Maranzana et al. [18] underlined the growing importance of conduction effects with reduction in the microchannel size. Kroeker et al. [19] investigated numerically the three-dimensional fluid flow and conjugate heat transfer in heat sinks with circular microchannels. They showed that the heat flux is much higher near the inlet of the channel owing to axial conduction. As a result, the temperature in both the fluid and solid regions was found to exhibit a high gradient in the entrance region.

The present paper is devoted to the numerical modeling of the flow and heat transfer in microchannels and is focused on the coupling of axial heat conduction in the walls with convection in the microchannels. Associated entrance effects are of special interest because they are probably significant in many published data. This study pertains to experimental investigations of Gao et al. [6] conducted in large-span rectangular microchannels, which have revealed a significant reduction in the Nusselt number for microchannel spacing less than 500 μm. The geometry considered in the present numerical simulations is as close as possible to the physical situation. It is therefore possible to compare numerical and experimental results and to test the relevance of conduction/convection coupling effects and associated entrance effects in the deviation of heat transfer results from the macroscale laws.

2. Experimental set-up

In the experimental set-up, the active channel walls were two hand-polished plane bronze blocks, which were separated by a stainless plate (of thickness e) with a hollowed out central part of width w (see dimensions in Fig. 1). Two sumps were machined in these blocks at channel inlet/outlet. Details of the facility may be found in Gao et al. [6]. The spacing e of the microchannel test section was determined by the plate thickness, which could be varied in the range 0.1–1 mm by steps of 0.1 mm. The main advantage of this arrangement is that the channel walls are represented by the same surfaces and that only the channel spacing is varied during all the experiments. Also, for this configuration of a large-span unique channel ($25 < w/e < 250$), experimental results are more easily compared to theory and numerical analysis than in multiple-channel arrangement. Heating was provided by four electric cartridges, which were inserted inside the two blocks and surrounded by an insulating material. The inlet/outlet water temperatures (T_{in}, T_{out}) were measured inside the upstream/downstream sumps, then the fluid bulk temperature T_f distribution in the microchannel was approximated as a linear one. It is worth noting that the heater is noticeably shorter than the microchannel length (approximately 25%), what contributed to the non-uniform heat flux distribution (see Section 4.2 for details). Four thermocouples were mounted along the microchannel in the plane of symmetry with their tips located 1 mm away from the microchannel surface. Two pressure transducers were flush-mounted in the wall of the inlet/outlet containers. It is worth underlining that the two blocks are rounded off in the upstream part so as to form a convergent channel entrance, contrary to several other studies where the channel inlet is characterized by an abrupt contraction. As a consequence, the head losses were neglected in the converging inlet channel and were assumed to be concentrated at the channel outlet. Thus, the pressure at the microchannel entrance was corrected by the inertia term accounting for flow

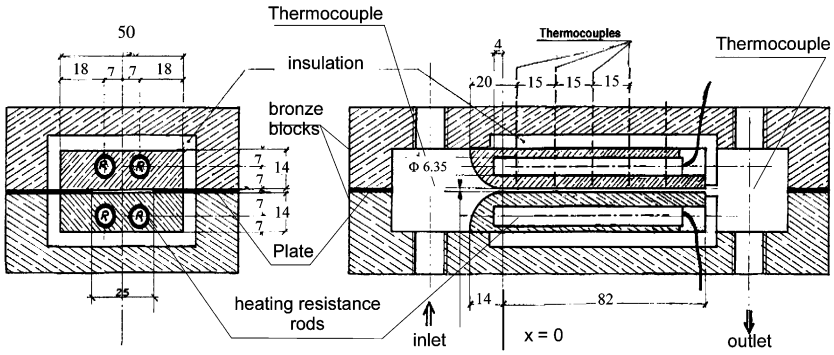

Fig. 1. Sketch of the test section.

acceleration in the convergent channel and no correction was done on the outlet pressure. The data were interpreted by using the Reynolds number *Re* and the Nusselt number *Nu*, both based on the hydraulic diameter D_h. The water properties, such as density, dynamic viscosity and *Pr* number were determined at the average inlet/outlet temperature. The thermal conductivity used in *Nu* definition was determined at the local film temperature T_{film} (average of wall and fluid bulk temperatures).

Since measurements of the local heat flux φ were not possible in the experimental study of Gao et al. [6], the authors assumed that the power density dissipated into the test section was uniformly distributed in a plane parallel to the active microchannel surfaces. The distance between the two planes ($e_s = 3.8$ mm) was determined by the position of the heating resistances. A one-dimensional model was used to account for the axial conduction effects in the slab delimited by the two planes. Results from the experimental investigations showed that the longitudinal distribution of *Nu* as given by Shah and London ([20], referenced as SL hereafter) is reasonably recovered for the channels of largest spacing in the laminar regime. However, for $e < 500\,\mu$m, a significant decrease in *Nu* was observed for reduced channel size. For $e = 0.1$ mm, *Nu* was about 60% smaller than the conventional value obtained in large-scale channels.

3. Numerical model

3.1. Computation domain, physical equations and boundary conditions

The geometry of the microchannel heat sink shown in Fig. 1 followed the details of the experimental set-up. Taking advantage of the symmetry of the experimental facility, the numerical model was represented by half of the actual geometry. The heat transfer process occurring in such a complex geometry consists of coupled conduction in the solid and forced convection by the cooling fluid. The model used the conventional mass, momentum and energy equations [21]. The equations were simplified by the following assumptions:

(1) fluid incompressibility,
(2) laminar flow character,
(3) negligible radiation heat transfer,
(4) negligible buoyancy,
(5) constant fluid and solid properties,
(6) negligible viscous heating.

The resulting equations are

$$\nabla \vec{V} = 0 \tag{1}$$

$$\rho_f(\vec{V}\cdot\nabla\vec{V}) = -\nabla p + \mu_f \nabla^2 \vec{V} \tag{2}$$

$$\rho_f C_{pf}(\vec{V}\cdot\nabla T) = \lambda_f \nabla^2 T \tag{3}$$

for the fluid and

$$\nabla^2 T = 0 \tag{4}$$

for the solid. Because of the assumptions of constant fluid properties and negligible buoyancy, the mass and momentum equations were not coupled with the energy equation. Therefore, the temperature field was calculated by solving the energy equation after the converged solution for the flow field was obtained. Such an approach allowed to significantly speed up the computational convergence. The simulations were conducted both for two- and three-dimensional cases. The simplified two-dimensional geometry was used for extensive tests of computational mesh and for the validation of the numerical model with data reported in the open literature. For the three-dimensional case the entire geometry was considered. The momentum and continuity equations were solved for the following hydraulic boundary conditions:

(1) a uniform velocity profile was set at the upstream sump inlet or, for the test cases, at the channel inlet,

(2) the flow was assumed to be fully developed at the test section exit plane (three-dimensional model) or at the channel exit plane (two-dimensional model). The numerical model assumed no axial gradient for all the flow variables except pressure in both cases.

The thermal boundary conditions were set as follows:

(1) either constant heat flux density at the walls of the heater cartridges (three-dimensional model, total heat flux $\Phi = 180\,\mathrm{W}$) or constant energy source inside the cartridge volume (two-dimensional model),
(2) free convection heat transfer with surrounding air at the outside walls of the test section; the assumed values of the heat transfer coefficient and ambient temperature were equal to $10\,\mathrm{W\,m^{-2}\,K^{-1}}$ and 300 K, respectively. These conditions were suggested by the experimental conditions. Quiescent conditions were kept in the laboratory during the experiments, so that the outer surface was assumed to be cooled only by free convection. It has been found that the heat exchange at the outer surface was of minor importance and that the corresponding heat transfer characteristics were not crucial in the model.

The x-direction runs along the channel with the axis origin located at the channel entrance downstream the converging region.

The flow and heat transfer characteristics depend on the channel Reynolds number Re, the Prandtl number and the test section geometry. This paper is focused on entrance effects and conduction effects on microchannel heat transfer, which may be tentatively quantified by the two following dimensionless parameters:

(1) Inlet conditions may be characterized by the ratio of channel height to boundary layer thickness δ_0 at the channel inlet. δ_0 is inversely proportional to the square root of the Reynolds number based on the length of the converging part of the channel entrance. Since the convergent channel entrance is formed by two quarters cylinder of radius R (= 14 mm, Fig. 1), R is chosen as the characteristic longitudinal length for the boundary layers developing on the convergent channel walls. Keeping the Reynolds number Re based on the microchannel hydraulic diameter, δ_0 is estimated by

$$\delta_0 \sim \sqrt{\frac{eR}{Re}} \tag{5}$$

The dimensionless channel height is then defined as

$$e^* = \sqrt{\frac{e \cdot Re}{R}} \tag{6}$$

(2) Conduction effects may be quantified by the dimensionless parameter

$$M = \frac{\lambda_s \frac{e_s}{L}}{\rho c_f e_f V_b} \tag{7}$$

first proposed by Peterson [17] and used by Maranzana et al. [18] in a quasi-analytical computation of conjugated heat transfer in microchannels. M is the ratio of typical heat flux of longitudinal conduction in the wall to convective heat flux across the channel. The transverse lengthscale for the conductive heat flux was chosen as the distance e_s (= 3.8 mm) from the bottom of the heating elements to the channel wall. The experiments of Gao et al. [6] and the present numerical simulations were conducted with moderate values of Re leading to low values of M. For the conditions of this study, $M < 0.01$ so that the coupling between convection in microchannels and conduction in the walls was weak.

Numerical computations of the flow were carried out by using the commercial code Fluent 5.4. The equations were discretized by means of a second order upwinding finite volume method. As these equations are non-linear, a semi implicit pressure linked equations (SIMPLE) algorithm was used. This algorithm is based on a prediction-correction method, which allows the equations to be linearized and solved iteratively. The pressure under-relaxation factor was set to 0.3.

Meshing was performed by using Gambit 1.3. Due to the very complex geometry corresponding to the experimental test section, the computation domain was split into several regions. Details may be found in [22]. The domain corresponding to the solid block was meshed using unstructured mesh. Structured mesh was utilized for the inlet/outlet containers and the microchannel. Tests were conducted for the flow and heat transfer in the microchannel, which was the most critical part of the test section for numerical accuracy. Typical two-dimensional cases were considered with $e = 1$ mm and a uniform inlet velocity profile ($Re = 1625$). The level of normalized residuals for x and y velocity components reached 10^{-7} for both quantities after 350 iterations for a grid of 40×328 nodes. The level of normalized residual corresponding to mass imbalance reached 2×10^{-4} after 100 iterations in the same conditions. The variation of the pressure drop across the microchannel was about 0.2% when the number of nodes was increased from 30 to 40 in the crosswise direction for 80 nodes in the streamwise direction. Negligible variations of the total pressure drop were observed when the number of nodes was increased from 80 to 164 in the streamwise direction. The variation of the mass flow rate in the beginning of the channel was more sensitive to the number of nodes in the streamwise direction. It was necessary to use 328 nodes in the streamwise direction to reduce the variation of the mass flow rate to 2% in the very beginning of the channel ($x/L < 0.02$).

The total number of cells was optimized from series of tests and equal to about 2×10^6 (2.7×10^6) for $e = 1$ (0.3) mm. The number of mesh nodes used in the microchannel by the numerical calculations was equal to $164\times30\times20$ for $e = 1$ mm in the streamwise, crosswise and spanwise directions, respectively. Special care had to be taken with the cell aspect ratio especially in the entrance region of the test section, i.e. for the rapidly developing flow. For $e = 0.3$ mm, it was necessary to reduce the length of the mesh elements so that 300 nodes were used along the channel. In order to avoid a too large number of nodes, the grid applied in the microchannel entrance was non-uniformly distributed in x-direction. For all the cases considered, the grid was individually adopted and it was checked that the solution was mesh-independent.

3.2. Model validation

The numerical model was checked for laminar simultaneously thermally and hydraulically developing flow along a two-dimensional channel with symmetrical uniform heat flux surfaces. We used for comparison the results of Hwang and Fan [23] reported by SL and fitted by Bejan and Sciubba [24] using empirical formulas of the Churchill and Usagi [25] type. For $Pr = 0.7$, the local Nusselt number is given by

$$Nu = \frac{\varphi\cdot D_h}{(T_w - T_f)\lambda} = \left[\left(0.587(x^*)^{-\frac{1}{2}}\right)^3 + 8.235^3\right]^{\frac{1}{3}} \tag{8}$$

where the dimensionless abscissa is

$$x^* = \frac{x}{D_h Re}\frac{1}{Pr} \tag{9}$$

Eq. (8) assumes uniform inlet velocity and temperature profiles, i.e. it takes into consideration the so-called entrance effect. Fig. 2 shows an excellent agreement of the present simulation with Eq. (8). The same good agreement was found for $Pr = 10$. This provides confidence in the numerical technique and therefore in the results produced with the current numerical approach.

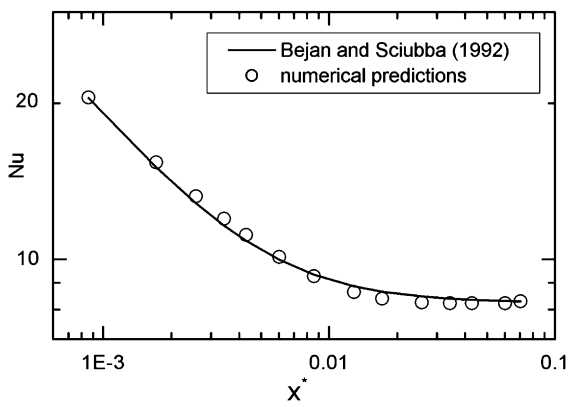

Fig. 2. Uniform inlet velocity and temperature profiles and uniform heat flux. Variation of Nusselt number along the channel ($Pr = 0.7$, $Re = 832$, $e = 1$ mm). Comparison with Bejan and Sciubba's formula [24].

4. Results

4.1. Hydraulic properties

Shah and London [20] presented a comprehensive review of laminar forced convection in ducts of various cross-sections, including rectangular channels. Their results were used as the reference in this part of the study.

The Fanning friction factor f is related to the pressure drop Δp over the hydrodynamically developing length x via

$$f = \frac{\Delta p}{2\rho V_b^2}\frac{D_h}{x} \tag{10}$$

The Poiseuille number is defined as

$$Po = fRe \tag{11}$$

For laminar developing flow in two-dimensional channels of usual size, SL proposed the following formula

$$Po_{lam}(x^+) = \frac{3.44}{\sqrt{x^+}} + \frac{24 + \frac{0.674}{4x^+} - \frac{3.44}{\sqrt{x^+}}}{1 + \frac{2.9\times10^{-5}}{x^{+2}}} \tag{12}$$

where the dimensionless coordinate is defined as

$$x^+ = \frac{x}{D_h Re} \tag{13}$$

Fig. 3 shows the variations of the Poiseuille number against x^+ for the two microchannel spacings considered in this study. For the complex geometry of the numerical

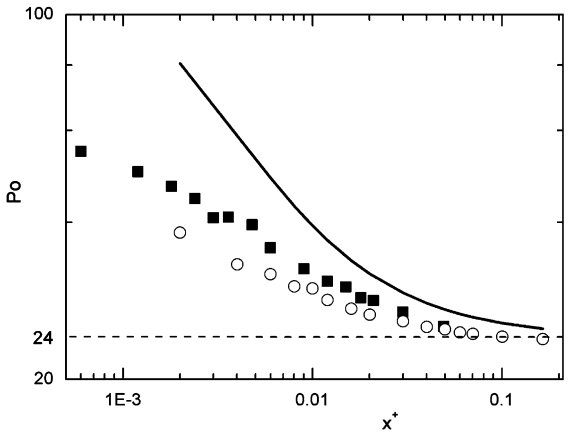

Fig. 3. Variation of Poiseuille number along the channel. Influence of inlet velocity profile. (■) $e = 1$ mm, $Re = 865$, $e^* = 7.9$; (○) $e = 0.3$ mm, $Re = 842$, $e^* = 4.2$.

simulation (including inlet container), *Po* values are significantly smaller than predicted by SL. This is obviously due to the finite thickness of the boundary layers at the channel entrance, as opposed to a uniform velocity profile in the SL reference case. Furthermore, the distribution of *Po* depends on *Re* and channel spacing separately, contrary to SL reference case where x^+ is the proper dimensionless group. As a result, the distributions of $Po(x^+)$ are different for the two channel spacings as shown in Fig. 3. It then turned out that the computations for a given value of *Re* provide only one point (corresponding to the particular value of $x^+ = L/(D_h Re)$) for comparison with the experimental data for which the pressure is measured at channel inlet/outlet. It can also be observed that the entrance effect is reduced when the dimensionless spacing e^* decreases from 7.9 to 4.2, as expected. Both distributions tend to the asymptotic value of laminar fully developed flow ($Po = 24$).

4.2. Heat transfer

Bronze was used as the material of the solid blocks because the simulation had to be consistent with the experiments. Some calculations were carried out, however, with brass as solid material of significantly higher conductivity, but the same tendencies were found for the heat transfer characteristics. The Prandtl number was set to $Pr = 6$.

Fig. 4 shows the temperature distribution in the plane of symmetry. The region of the highest temperature gradients corresponds to the presence of the microchannel insulation. It is worth emphasizing that insulation does not completely surround the bronze blocks. There is a gap near the convergent channel (Fig. 1) allowing a part of the heat flux to be conducted to the surrounding blocks. That in turn leads to: (i) additional heat transfer to water in the inlet container and (ii) increased heat losses to ambient air. Fig. 4 shows that the wall temperature decreases in the last part of the microchannel ($x/L > 0.73$) due to the lack of heating in this region.

The local *Nu* number is defined as

$$Nu = \frac{h \cdot D_h}{\lambda} \tag{14}$$

where the convection heat transfer coefficient h is given by

$$h = \frac{\varphi}{T_w - T_f} \tag{15}$$

Two-dimensionality checks showed that the wall heat flux φ_{num} varied less than 5% over 80% of the span. As a consequence, the wall heat flux, the wall and local fluid bulk temperatures (respectively, T_w, T_f) were taken in the plane of symmetry of the flow.

The numerical heat flux φ_{num} was normalized by the value φ_{exp} corresponding to uniform distribution over the heating surface, as it was assumed during experiments. The three following regions may be observed on Fig. 5:

(1) the microchannel entrance where φ_{num} first decreases because the velocity and temperature boundary layers are growing in this part of the channel,
(2) the middle part of the microchannel ($0.1 < x/L < 0.7$) where φ_{num}-variations are less than 6%,
(3) the exit part (around 30% of the channel length) where φ_{num} strongly decreases due to the lack of heating and to conduction in the solid blocks. It is worth underlining that the length of the heating elements is about 25% smaller than the channel length (Fig. 1). As a result, the last part of the solid blocks is intensively cooled by the flow, giving rise to longitudinal conduction along the wall in the downstream direction. The heat flux exchanged with the fluid is, however, obviously lower than in the upstream region owing to the lack of heating source.

The assumption used in the experiments neglected heat transfer in inlet and outlet containers. This explains

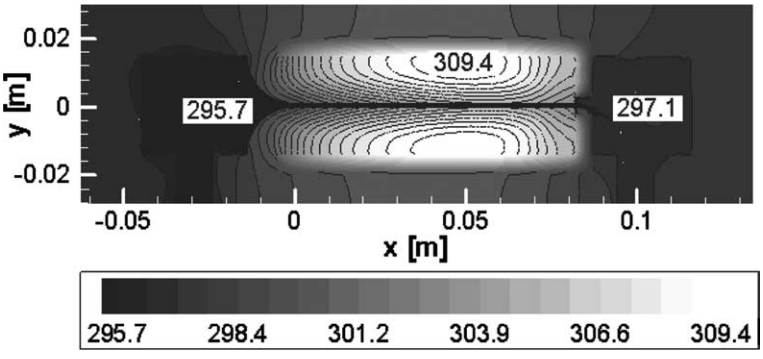

Fig. 4. Temperature distribution in the plane of symmetry. $e = 1$ mm. $Re = 2166$, $e^* = 12.4$, $\Phi = 180$ W. Scale given in K.

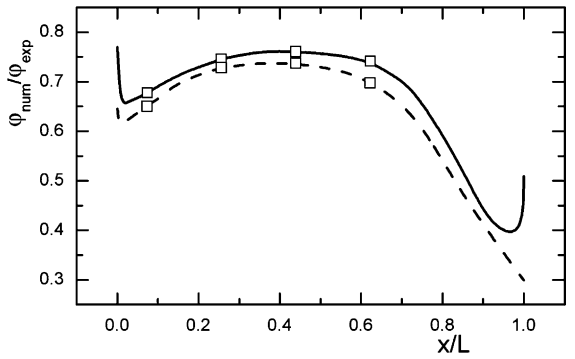

Fig. 5. Variation of dimensionless wall heat flux along the channel. (---) $e = 1$ mm, $Re = 2166$, $e^* = 12.4$; (—) $e = 0.3$ mm, $Re = 2061$, $e^* = 6.6$, (□) thermocouples position.

why the numerical heat flux is smaller than φ_{exp} and, moreover, is non-uniformly distributed. Table 1 gives the distribution of heat fluxes in the different regions of the test section for $e = 1$ mm. Very similar results were obtained for $e = 0.3$ mm. A significant part of the power supplied by the electric heating is transferred to water via the inlet sump and the convergent channel. It may be remarked that this heat flux is eventually transferred to the flow by the inlet container and convergent channel walls. This explains why a close agreement was found in the experiment [6] for the electric power dissipated in the test section and the total rate of enthalpy convected by the stream across the channel, which was determined with the fluid temperatures in the inlet/outlet sumps (Fig. 1).

Fig. 6 illustrates the variations of Nu against the dimensionless coordinate defined by Eq. (9). The numerical results are compared with the data obtained for uniform inlet velocity and temperature profiles and $Pr = 6$. This reference curve allows to identify and quantify the entrance effect. The Nusselt number was calculated along the channel for three values of the Reynolds number. Each curve in Fig. 6 corresponds to a particular value of Re. As can be seen in Fig. 6, the particular curves are clearly Re-dependent revealing relative shifts

Table 1
Distribution of percentage heat fluxes in the various regions of the test section, $e = 1$ mm

%	$Re = 518$, $e^* = 6.1$	$Re = 865$, $e^* = 7.9$	$Re = 2076$, $e^* = 12.2$
Heat losses	3.2	2.2	1.2
Inlet sump	18.5	17.5	15.5
Convergent channel	9.7	9.5	9.5
Microchannel	64	65	67
Outlet sump	4.6	5.8	6.8

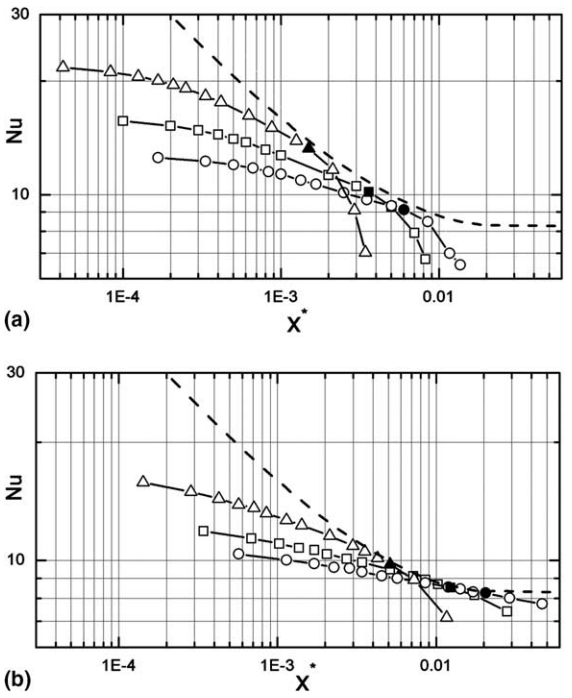

Fig. 6. Variation of Nusselt number along the channel for two channel spacings: (---) uniform inlet conditions; (●, ■, ▲) $x/L = 0.44$; (a) $e = 1$ mm, (○) $Re = 518$, $e^* = 6.1$; (□) $Re = 865$, $e^* = 7.9$; (△) $Re = 2076$, $e^* = 12.2$; (b) $e = 0.3$ mm, (○) $Re = 506$, $e^* = 3.3$; (□) $Re = 842$, $e^* = 4.2$; (△) $Re = 2023$, $e^* = 6.6$.

and intersections. The differences between these curves can obviously be explained by the Re-dependent velocity and temperature profiles in the boundary layers at the microchannel entrance. For uniform inlet velocity and temperature profiles, Nu depends on x^*, not on x and Re separately. This is obviously not true for the present model which takes conduction and complex geometry effects into account. As for the friction factor, the entrance effect increases with the Reynolds number and e^* because the velocity/temperature profiles are closer to uniform distribution.

The data may also be presented for a fixed value of x and varying Re, as in the experimental procedure. In this case, only three points are available for a given value of x, since each curve in Fig. 6 was obtained for a given value of Re and varying x. As an example, Fig. 6 shows the variation of Nu at $x/L = 0.44$ (solid symbols). The comparison between the reference curve and the marked numerical points for this particular position in the microchannel allows for the following observations:

(1) the entrance effect is slightly weaker for the present results than for the reference case when

$e = 1$ mm. This is due to a non-uniform temperature profile at channel inlet, as described before,
(2) the convergence of data points and the reference curve when $e = 0.3$ mm indicates that the entrance effect is so weak at this position in the channel that Nu is no more sensitive to the inlet conditions,
(3) the entrance effect is reduced for lower channel spacing, as expected.

5. Comparison of experimental results with numerical predictions

The dimensionless temperature θ was defined as

$$\theta = \frac{T - T_{in}}{\frac{\varphi_{num} \cdot D_h}{\lambda}} \tag{16}$$

The normalization of temperatures by φ_{num} was chosen to reduce the non-linearity of T_f due to the variations of φ_{num}, especially near the channel entrance. The numerical solution for θ is considered at the location of the thermocouples.

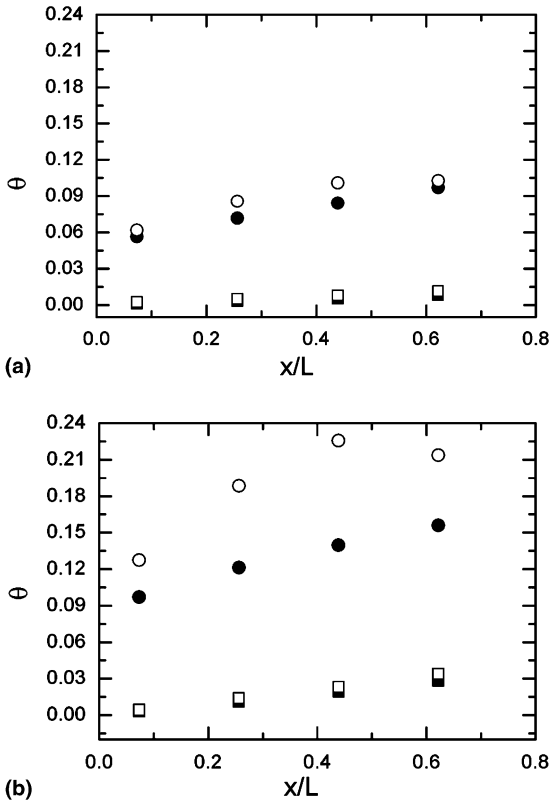

Fig. 7. Variation of wall and fluid temperatures along the channel. Comparison between numerical and experimental results for two channel spacings: (■) $\theta_{f_{num}}$, (●) $\theta_{s_{num}}$, (□) $\theta_{f_{exp}}$, (○) $\theta_{s_{exp}}$ (a) $e = 1$ mm, $Re = 2166$, $e^* = 12.4$; (b) $e = 0.3$ mm, $Re = 2061$, $e^* = 6.6$.

Fig. 7 shows the distribution of θ along the channel both for fluid and solid domains. Comparison between experimental results and numerical predictions for the water bulk temperature (squares in Fig. 7) shows that discrepancies are relatively small. The assumption of linear variation of T_f is rather well verified. It may be remarked that the thermocouples are located in the region where the variations of φ_{num} are relatively small (Fig. 5). One can see that larger discrepancies occur in the solid region (circles in Fig. 7) resulting in higher values of the difference $T_w - T_f$ for the experimental results. The uncertainty of measured temperatures was estimated to be 0.1 K [6], which corresponds to a normalized uncertainty of 10^{-4} on θ. For $e = 1$ mm ($e^* = 12.4$), the discrepancies between experimental and numerical results vary from about 5% to 18% with reference to experimental data, while for $e = 0.3$ mm ($e^* = 6.6$) they are larger and reach about 40%. In this latter case, they account for the decrease in Nu observed in the experiments.

The location of the thermocouple tips could noticeably decrease the values of Nu, especially for small microchannel spacings, owing to finite temperature gradients in the solid blocks. Nu was calculated in the experiments [6] with the temperature given by the thermocouples, which were about 1 mm away from the liquid/solid interface. In order to eliminate the influence of the thermocouples position in the determination of Nu, the experimental temperature was corrected using the wall temperature gradient in the solid as computed by the numerical solution. Furthermore, the actual wall heat flux is probably close to the numerical value. Consequently, the experimental Nusselt number was recalculated with the numerical heat flux for want of a better estimation of φ. Fig. 8 compares the numerical and experimental results of Nu for $Re \approx 2100$. It should be noted that only the second and third thermocouples ($x/L = 0.256$ and 0.44) were considered in the experimental Nu values because they correspond to the region of nearly uniform heat flux.

For $e = 1$ mm ($e^* = 12.4$), which may be considered as a conventional size for a channel flow, above comparisons indicate that:

(1) the heat flux is significantly overestimated (about 25%) by the assumption used in the experiments corresponding to negligible heat transfer in inlet/outlet containers (Fig. 5),
(2) the wall temperature is slightly underestimated by the numerical model (Fig. 7a),
(3) Nu is slightly overestimated (about 10–20%) by the numerical model when Nu_{exp} is calculated with φ_{num}.

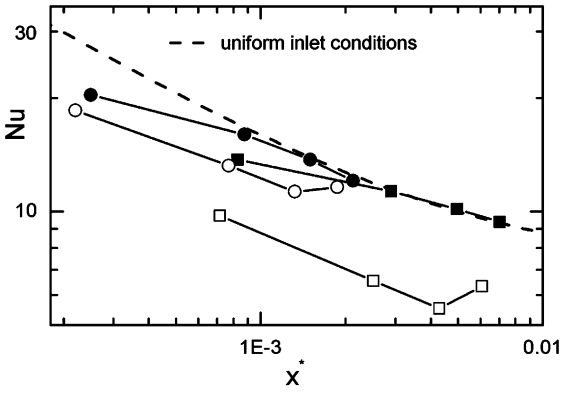

Fig. 8. Variation of Nusselt number along the channel. Comparison between numerical and experimental data. $e = 1$ mm, $Re = 2166$, $e^* = 12.4$, (○) Nu_{exp}, (●) Nu_{num}; $e = 0.3$ mm, $Re = 2061$, $e^* = 6.6$, (□) Nu_{exp}, (■) Nu_{num}.

For $e = 0.3$ mm ($e^* = 6.6$), comparisons show that:

(1) the heat flux φ_{num} distribution is the same as in the previous case (Fig. 5),
(2) the wall temperature is much higher than the numerical solution (Fig. 7b),
(3) the Nusselt number Nu_{exp} is significantly lower (about 40–80%) than the numerical value.

An important conclusion is therefore that the observed reduction in Nu_{exp} cannot be accounted for by conduction effects, which would have distorted the temperature field and the corresponding heat flux distribution. This result is consistent with the estimation of conduction effects as quantified by the dimensionless parameter M. In the present experiments, $M < 0.01$ so that conduction effects and wall conduction/convection coupling are weak in the middle part of the channel. They are probably concentrated in the last part of the channel as explained in Section 4.2 and in the entrance region owing to the lack of insulating material (see the pattern of isotherms in Fig. 4). As a result, φ_{num} is rather uniformly distributed in the middle part of the microchannel, but at a level significantly lower than φ_{exp} due to conduction toward the upstream and downstream containers (Table 1). Conduction effects would have been much stronger for flows at very low Re, as shown in [18]. Fig. 8 shows that the reduction in Nu_{exp} is not explained by the present numerical simulation. The model proposed by Qu et al. [4] is based on the wall roughness effect and does not apply in the present study since the measured wall roughness is less than 0.1 μm. Possible explanations can be proposed as follows:

(1) the model neglected the variations of the fluid physical properties which can modify the convective heat transfer,
(2) possible sources of error in the experiments cannot be definitely discarded. For example, thermal expansion of the solid blocks could affect the channel spacing. New experiments are planned to check this hypothesis.

6. Two-dimensional numerical simulations

The simulation performed for two-dimensional geometry could bring obvious advantages as reduction in computer running time and simplification of the modeled geometry. This section compares results obtained in two- and three-dimensional numerical simulations. The computations were achieved for the two extreme channel spacings used in the experiments, i.e. 0.1 mm and 1 mm, with the corresponding Re number and e^* ranges:

$$Re \in (200\text{–}2166), \quad e^* \in (3.8\text{–}12.4) \quad \text{for } e = 1 \text{ mm}$$

$$Re \in (500\text{–}3000), \quad e^* \in (1.9\text{–}4.6) \quad \text{for } e = 0.1 \text{ mm}$$

Fig. 9 shows a perfect agreement between Nu distributions obtained with the two- and three-dimensional models. This suggests an application of two-dimensional model for further quantitative investigations.

6.1. Hydraulic properties

Three-dimensional simulations have shown that the Poiseuille number should be determined as a function of Re for given channel length L and spacing e, since the entrance effect was found to be Re-dependent. As a consequence, the present computations were achieved for given values of L and e and varying Re, contrary to three-dimensional simulations. It is, however, presented in Fig. 10 against L^+ (= $L/(D_h Re)$), in consistency with the reduction of experimental data. As can be seen

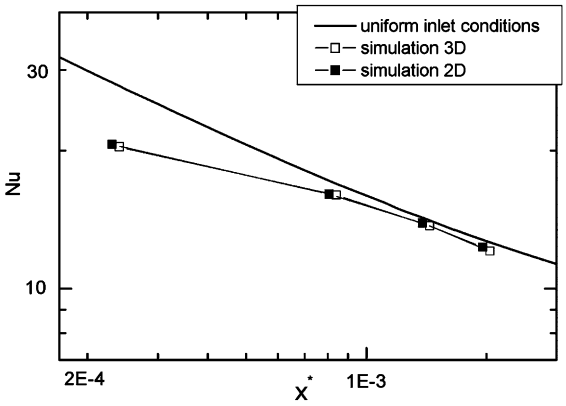

Fig. 9. Comparison of Nusselt number distributions along the channel between two and three-dimensional models. $e = 1$ mm, $Re = 2166$, $e^* = 12.4$.

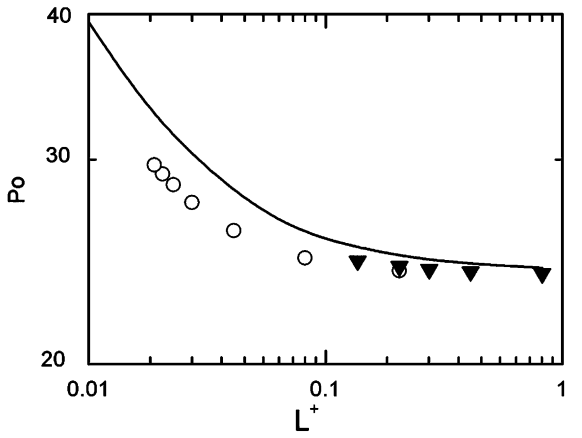

Fig. 10. Poiseuille number as a function of dimensionless channel length $L^+(Re)$. (—) Shah and London [20], (○) $e = 1$ mm, (▼) $= 0.3$ mm.

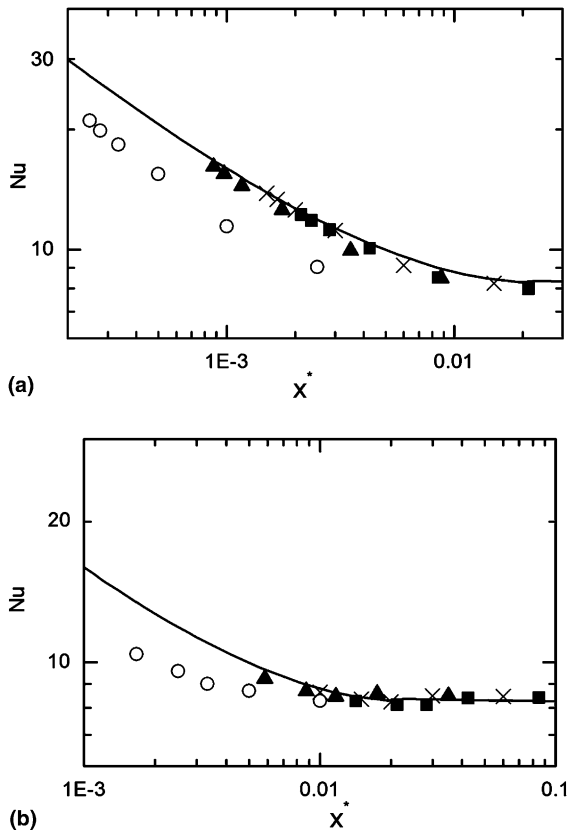

Fig. 11. Variation of Nusselt number along the channel for two channel spacings: (—) uniform inlet conditions. Position corresponding to thermocouple (1) (○), (2) (▲), (3) (×), (4) (■), (a) $e = 1$ mm (b) $e = 0.1$ mm.

in Fig. 10, the numerical results show a consistent distribution of $Po(L^+)$ which is located below SL curve, as predicted by the three-dimensional model and explained previously.

Entrance effects are found to be negligible when L^+ is higher than about 0.1 with corresponding values of the Re number:

$Re = 300$ for $e = 1$ mm

$Re = 3000$ for $e = 0.1$ mm

The two sets of numerical results then overlap.

6.2. Heat transfer

Fig. 11 shows the variations of Nu along the channel for the same two extreme channel spacings ($e = 1$ mm and $e = 0.1$ mm). Computations were achieved by varying the Reynolds number as for hydrodynamics (ranges are given in previous subsection). Nu was estimated in the sections of the four thermocouples (respectively $x/L = 0.073$, 0.256, 0.44, 0.62) with the temperature at the fluid/solid interface. One can observe that Nu values are well fitted to the reference curve except for the data corresponding to the section of the first thermocouple (open circles in Fig. 11). For the conditions of the numerical simulation, Nu is therefore affected on a short distance by the finite thickness of the thermal boundary layer at channel entrance.

7. Conclusions

The three-dimensional flow and associated heat transfer in a rectangular microchannel heat sink were analyzed numerically. The geometry of the test section used in the experiments of Gao et al. [6] was taken into account in two- and three-dimensional computations. The numerical simulation considered the coupling between convection in microchannels and conduction in the walls and in the complete solid material. The local heat transfer characteristics, i.e. temperature, heat flux and Nusselt number, were obtained. The key findings of the present study are as follows:

(1) the results of numerical simulations using the continuum model (conventional mass, Navier–Stokes and energy equations) are in good agreement with published data on flow and heat transfer in two-dimensional channels,
(2) two- and three-dimensional computations are in perfect agreement for the model used in the present study,
(3) the thermal characteristics show that entrance effects are dependent on the Reynolds number and the channel spacing separately, contrary to

the reference case of uniform inlet velocity and temperature profiles, such as reported by Shah and London [20],

(4) numerical simulations turned out to be very helpful as a complement to the interpretation of experimental data, where complex measurements of heat flux and temperature field are obviously not possible,

(5) the numerical models used in this work assumed some simplifications e.g. did not take into account viscous heating, which could decrease the Nusselt number especially for channels of smaller spacing than those investigated in the current work,

(6) the present numerical simulations show that there is no size effect on heat transfer when the channel spacing is reduced from 1 mm down to 0.1 mm. As a result, the strong reduction in the Nusselt number observed in experiments cannot be explained by conduction effects due to the complex geometry, like axial conduction in the walls or lack of two-dimensionality of the heat flux distribution. Further investigations are planned both from the numerical and experimental points of view in order to reduce the gap between the results of the two approaches.

Acknowledgments

This research was supported by the CNRS and Rhône-Alpes Region. The authors would like to gratefully acknowledge Socrates organization for supporting the visit of Gabriel Gamrat in Grenoble.

References

[1] D.B Tuckerman, R.F. Pease, High-Performance heat sinking for VLSI, IEEE Electron Dev. Lett., EDL-2 5 (1981) 126–129.

[2] C.B. Sobhan, S.V. Garimella, A comparative analysis of studies on heat transfer and fluid flow in microchannels, Microscale Thermophys. Eng. 5 (2001) 293–311.

[3] X.F. Peng, G.P. Peterson, B.X. Wang, Heat transfer characteristics of water flowing through microchannels, Exp. Heat Transfer 7 (1994) 265–283.

[4] W. Qu, Gh.M. Mala, D. Li, Heat transfer for water flow in trapezoidal silicon microchannels, Int. J. Heat Mass Transfer 43 (2000) 3925–3936.

[5] G.P. Celata, M. Cumo, M. Guglielmi, G. Zummo, Experimental investigation of hydraulic and single-phase heat transfer in 0.130-mm capillary tube, Microscale Thermophys. Eng. 6 (2002) 85–97.

[6] P. Gao, S. Le Person, M. Favre-Marinet, Scale effects on hydrodynamics and heat transfer in two-dimensional mini and microchannels, Int. J. Therm. Sci. 41 (2002) 1017–1027.

[7] A. Weisberg, H.H. Bau, J.N. Zemel, Analysis of microchannels for integrated cooling, Int. J. Heat Mass Transfer 35 (1992) 2465–2474.

[8] D.B. Tuckerman, Heat Transfer Microstructures for Integrated Circuits, Ph.D. thesis, Stanford University 1984.

[9] K.C. Toh, X.Y. Chen, J.C. Chai, Numerical computation of fluid flow and heat transfer in micro-channels, Int. J. Heat Mass Transfer 45 (2002) 5133–5141.

[10] A.G. Fedorov, R. Viskanta, Three-dimensional conjugate heat transfer in the micro-channel heat sink for electronic packaging, Int. J. Heat Mass Transfer 43 (2000) 399–415.

[11] W. Qu, I. Mudawar, Analysis of three-dimensional heat transfer in micro-channel heat sinks, Int. J. Heat Mass Transfer 45 (2002) 3973–3985.

[12] W. Qu, I. Mudawar, Experimental and numerical study of pressure drop and heat transfer in a single-phase microchannel heat sinks, Int. J. Heat Mass Transfer 45 (2002) 2549–2565.

[13] I. Tiselj, G. Hetsroni, B. Mavko, A. Mosyak, E. Pogrebnyak, Z. Segal, Effect of axial conduction on the heat transfer in micro-channels, Int. J. Heat Mass Transfer 47 (2004) 2551–2565.

[14] D. Lelea, S. Nishio, K. Takano, The experimental research on microtube heat transfer and fluid flow of distilled water, Int. J. Heat Mass Transfer 47 (2004) 2817–2830.

[15] M.G. Mala, D. Li, J.D. Dale, Heat transfer and fluid flow in microchannels, Int. J. Heat Mass Transfer 40 (1997) 3079–3088.

[16] Z.Y. Guo, Z.X. Li, Size effect on microscale single-phase flow and heat transfer, Int. J. Heat Mass Transfer 46 (2003) 149–159.

[17] R.B. Peterson, Numerical modeling of conduction effects in microscale counterflow heat exchangers, Microscale Thermophys. Eng. 3 (1999) 17–30.

[18] G. Maranzana, I. Perry, D. Maillet, Mini- and microchannels: influence of axial conduction in the walls, Int. J. Heat Mass Transfer 47 (2004) 3993–4004.

[19] C.J. Kroecker, H.M. Soliman, S.J. Ormiston, Three-dimensional thermal analysis of heat sinks with circular cooling micro-channels, in: 1st Int. Conference on Microchannels and Minichannels, Rochester, New York, USA, April 24–25, 2003, pp. 731–738.

[20] R.K. Shah, A.L. London, Laminar flow forced convection in ducts, in: Advanced Heat Transfer, Academic Press, New York, 1978 (Chapter 6).

[21] A. Bejan, Convection Heat Transfer, second ed., John Wiley & Sons, New York, USA, 1995.

[22] G. Gamrat, Numerical modeling of heat transfer in microchannels, MSc Report, University of Czestochowa, Poland, 2003.

[23] C.L. Hwang, L.T. Fan, Finite difference analysis of forced-convection heat transfer in entrance region of a flat rectangular duct, Appl. Sci. Res. 13 (1964) 401–422.

[24] A. Bejan, E. Sciubba, The optimal spacing of parallel plates cooled by forced convection, Int. J. Heat Mass Transfer 35 (1992) 3259–3264.

[25] S.W. Churchill, R. Usagi, A general expression for the correlation of rates of transfer and other phenomena, AIChE J. 18 (1972) 1121–1128.